Repeatability of ^{18}F-FDG PET radiomic features: A phantom study to explore sensitivity to image reconstruction settings, noise, and delineation method

Elisabeth Pfaehler[a)*]
Department of Nuclear Medicine and Molecular Imaging, Medical Imaging Center, University of Groningen University Medical Center Groningen, Groningen, The Netherlands

Roelof J. Beukinga[*]
Department of Nuclear Medicine and Molecular Imaging, Medical Imaging Center, University of Groningen University Medical Center Groningen, Groningen, The Netherlands
Department of Biomedical Photonic Imaging, University of Twente, Enschede, The Netherlands

Johan R. de Jong
Department of Nuclear Medicine and Molecular Imaging, Medical Imaging Center, University of Groningen University Medical Center Groningen, Groningen, The Netherlands

Riemer H. J. A. Slart
Department of Nuclear Medicine and Molecular Imaging, Medical Imaging Center, University of Groningen University Medical Center Groningen, Groningen, The Netherlands
Department of Biomedical Photonic Imaging, University of Twente, Enschede, The Netherlands

Cornelis H. Slump
MIRA Institute for Biomedical Technology and Technical Medicine, University of Twente, Enschede, The Netherlands

Rudi A. J. O. Dierckx
Department of Nuclear Medicine and Molecular Imaging, Medical Imaging Center, University of Groningen University Medical Center Groningen, Groningen, The Netherlands

Ronald Boellaard
Department of Nuclear Medicine and Molecular Imaging, Medical Imaging Center, University of Groningen University Medical Center Groningen, Groningen, The Netherlands
Department of Radiology & Nuclear Medicine, Amsterdam University Medical Centers Location VUMC, Amsterdam, The Netherlands

(Received 13 June 2018; revised 14 November 2018; accepted for publication 21 November 2018; published 28 December 2018)

Background: ^{18}F-fluoro-2-deoxy-D-Glucose positron emission tomography (^{18}F-FDG PET) radiomics has the potential to guide the clinical decision making in cancer patients, but validation is required before radiomics can be implemented in the clinical setting. The aim of this study was to explore how feature space reduction and repeatability of ^{18}F-FDG PET radiomic features are affected by various sources of variation such as underlying data (e.g., object size and uptake), image reconstruction methods and settings, noise, discretization method, and delineation method.
Methods: The NEMA image quality phantom was scanned with various sphere-to-background ratios (SBR), simulating different activity uptakes, including spheres with low uptake, that is, SBR smaller than 1. Furthermore, images of a phantom containing 3D printed inserts reflecting realistic heterogeneity uptake patterns were acquired. Data were reconstructed using various matrix sizes, reconstruction algorithms, and scan durations (noise). For every specific reconstruction and noise level, ten statistically equal replicates were generated. The phantom inserts were delineated using CT and PET-based segmentation methods. A total of 246 radiomic features was extracted from each image dataset. Images were discretized with a fixed number of 64 bins (FBN) and a fixed bin width (FBW) of 0.25 for the high and a FBW of 0.05 for the low uptake data. In terms of feature reduction, we determined the impact of these factors on the composition of feature clusters, which were defined on the basis of Spearman's correlation matrices. To assess feature repeatability, the intraclass correlation coefficient was calculated over the ten replicates.
Results: In general, larger spheres with high uptake resulted in better repeatability compared to smaller low uptake spheres. In terms of repeatability, features extracted from heterogeneous phantom inserts were comparable to features extracted from bigger high uptake spheres. For example, for an EARL-compliant reconstruction, larger and smaller high uptake spheres yielded good repeatability for 32% and 30% of the features, while the heterogeneous inserts resulted in 34% repeatable features. For the low uptake spheres, this was the case for 22% and 20% of the features for bigger and smaller spheres, respectively. Images reconstructed with point-spread-function (PSF) resulted in the highest repeatability when compared with OSEM or time-of-flight, for example, 53%, 30%, and 32% of

repeatable features, respectively (for unsmoothed data, discretized with FBN, 300 s scan duration). Reducing image noise (increasing scan duration and smoothing) and using CT-based segmentation for the low uptake spheres yielded improved repeatability. FBW discretization resulted in higher repeatability than FBN discretization, for example, 89% and 35% of the features, respectively (for the EARL-compliant reconstruction and larger high uptake spheres).

Conclusion: Feature space reduction and repeatability of ^{18}F-FDG PET radiomic features depended on all studied factors. The high sensitivity of PET radiomic features to image quality suggests that a high level of image acquisition and preprocessing standardization is required to be used as clinical imaging biomarker. *© 2018 The Authors. Medical Physics published by Wiley Periodicals, Inc. on behalf of American Association of Physicists in Medicine.* [https://doi.org/10.1002/mp.13322]

Key words: ^{18}F-FDG PET/CT radiomic features, delineation, image reconstruction settings

1. INTRODUCTION

^{18}F-fluoro-2-deoxy-D-Glucose (^{18}F-FDG) positron emission tomography (PET) has become part of the routine oncological diagnostic workup and has been applied for treatment response monitoring and prognosis due to its ability to noninvasively visualize organs and lesions. Although qualitative visual image assessment remains important for these purposes, it has a limited capability to objectively quantify tracer uptake. The most widely used semi-quantitative measures are the maximum, mean, and peak standardized uptake value (SUV_{max}, SUV_{mean}, and SUV_{peak}) and morphologically based imaging features, such as the metabolic tumor volume or total lesion glycolysis.[1–3] However, these features ignore the intratumoral ^{18}F-FDG spatial distribution.[4] The rapidly emerging field of 'radiomics' computes a large number of quantitative image features to characterize this intratumoral distribution or other tumor phenotypes such as shape.[5–7]

Even though radiomics has the potential to add valuable information to the visual image evaluation in various cancer types,[8] several challenges need to be addressed before radiomics can safely be implemented in the clinic. One of the key problems with generating a multitude of features is the risk of false-positive findings due to multiple testing. Moreover, numerous features may represent similar tracer uptake characteristics, and may therefore be correlated and redundant.[9] As models composed of redundant features may become unstable and difficult to interpret, it is required to reduce the feature space to a degree that is manageable for clinical use without losing important information. However, the identification of nonredundant features is challenging. Possible solutions to reduce the feature space would be the use of principal component analysis or (hierarchical) clustering, based on correlation analysis or distance metrics.[10] Another challenge facing radiomic features is the establishment of their measurement error (i.e., reproducibility, repeatability, and reliability). Several studies have shown that the majority of the ^{18}F-FDG PET radiomic features are sensitive to numerous sources such as image acquisition, reconstruction protocols, or delineation method.[9,11–19] Our study investigates the relationship of multiple confounding factors, including different activity uptake levels, thereby simulating tracers showing differences in uptake. For this purpose, two phantoms (the NEMA image quality (IQ) phantom and a phantom containing in-house designed 3D printed inserts simulating realistic heterogeneity uptake) were scanned. Multiple factors were varied in order to investigate the relationships between scanner and underlying data-dependent factors. In contrast to the most other studies, this study focuses on the impact of underlying data characteristics (contrast), image reconstruction methods and settings, noise, discretization method, and delineation method on specifically the dimensionality reduction as well as repeatability of ^{18}F-FDG PET radiomic features.

2. MATERIALS AND METHODS

2.A. Phantom Experiments

2.A.1. NEMA image quality phantom

The NEMA NU 2-2012 IQ phantom was used in this study consisting of a background volume of 9400 ml and six fillable spheres with inner diameters of 10, 13, 17, 22, 28, and 37 mm. The phantom was filled with different ^{18}F-FDG concentrations. Two scans with sphere-to-background ratios (SBRs) higher than one (about 10:1, 5:1), and two scans with a SBR lower than one (about 0.5:1, and 0.25:1) were acquired. The spheres were filled with 22.6, 10.87, 1.08, and 0.65 kBq/ml measured with a dosiscalibrator (Veenstra instruments, VDC 2.0.2), while the background was filled with 2.4, 2.26, 2.12, and 2.68 kBq/ml, respectively. All phantom scans were acquired as 70 min list-mode data on a PET/CT system (Biograph mCT-40 PET/CT, Siemens, Knoxville, TN, USA). The data were reconstructed to obtain a frame of 30, 60, 120, and 300 s. For every scan duration, nine additional frames were reconstructed such that they contained the same amount of counts, taking into account the decay of the tracer. Each dataset was reconstructed using iterative ordered subset expectation maximization (OSEM) algorithm (3 iterations, 24 subsets) and the vendor provided time-of-flight (TOF) iterative reconstruction method (3 iterations, 21 subsets). Furthermore, all scans were reconstructed with and without resolution modeling (or point-spread-function (PSF)). The data were reconstructed with an image matrix size of 256 × 256 × 111 and a voxel size of 3.01 × 3.01 × 2 mm. The TOF reconstructions with and without PSF were also obtained with a matrix size of 400 × 400 × 111 leading to a cubic voxel size of 2 mm, as a cubic voxel size is recommended for feature extraction.[8] A low-dose CT scan (80 kV, 30 mAs, and 2 mm slice thickness) of the phantom was generated in order to calculate the attenuation map of the PET image. To obtain quantitative PET data, images were corrected for attenuation, scatter, random coincidences, and normalization. Images were smoothed with Gaussian filters of 0, 2, 4, 6, and 8 mm full width at half maximum (FWHM) and were converted to SUV, so that the mean phantom background SUV was equal to 1.[20]

2.A.2. 3D printed phantom inserts

Additionally, a second phantom scan was performed. The spheres of the IQ phantom were replaced by three 3D printed inserts simulating heterogeneous uptake and realistic tumor shapes. The inserts were designed according to Non-Small-Cell-Lung-Cancer (NSCLC) tumors extracted from patient studies. The tumors were segmented from the images and scaled in order to make the printing possible. PET images of the 3D printed inserts are displayed in Fig. 1. To achieve heterogeneous uptake, the inserts consist of two separate compartments that can be filled with different activity solutions. All three inserts reflect a unique uptake pattern, including homogeneous uptake (tumor 1), heterogeneity uptake across two compartments (tumor 2), and a tumor containing a necrotic core (tumor 3). Tumor 1 yields a size of 40.3 mm × 44 mm × 54.5 mm (volume 46.05 ml), the upper and lower part of tumor 2 yield sizes of 33.9 mm × 37 mm × 30 mm (volume 10.75 ml), and 24.3 mm × 40.5 mm × 36.6 mm (volume 13.12 ml), respectively. While the outer part of tumor 3 and the necrotic core yield sizes of 56 mm × 54 mm × 65.1 mm (volume 65.35 ml) and 25 mm × 24 mm × 31 mm (volume 7.8 ml). Tumor 1, the lower part of tumor 2, and the outer part of tumor 3 were filled with an activity solution of 19.49 kBq/ml, the upper part of tumor 2 with 10.94 kBq/ml, and the large background compartment of the NEMA IQ phantom with 1.94 kBq/ml. The necrotic core of tumor 3 contained nonradioactive water. The phantom was also scanned on a Siemens Biograph mCT40. Images were reconstructed using the same parameters as the IQ phantom described above (see also Table I).

2.B. Segmentation

Spheres and 3D printed inserts were segmented using low-dose CT- and PET-based delineation methods. The CT-based volume of interest (VOI) of the spheres was generated by the manual placement of a sphere-shaped VOI with corresponding sphere diameter, while the 3D printed inserts were manually segmented using an in-house software developed for the analysis of PET images. The PET-based segmentations were generated with a region growing method using a connectivity of 26 voxels implemented in Matlab 2014b (Mathworks, Natick, MA, USA). For the high uptake spheres and the tumor-shaped inserts, the segmented region grew from the center voxel of the highest $\mathrm{SUV}_{\mathrm{peak}}$ seed point till voxel intensities became less than 41% of this $\mathrm{SUV}_{\mathrm{peak.}}$[20] Conversely, for the low uptake spheres the segmentation algorithm was inverted: the segmented region grew from the center voxel of the lowest $\mathrm{SUV}_{\mathrm{peak}}$ seed point till the voxel intensities became larger than a SUV of 0.59. To prevent excessive overestimation of the actual sphere volume, the PET-based segmentation was limited to a sphere volume of 300% of the CT-segmented sphere volume. As texture analysis in three dimensions requires the VOI to be specified in all three spatial dimensions, only those segmentations that

TABLE I. List of used reconstruction parameters.

Parameters	Variables
SBR	10:1, 5:1, 0.5:1, 0.25:1
Reconstruction	OSEM, TOF, PSF, PSFTOF
Matrix/voxel size	256 × 256 × 111 (3.1819 × 3.1819 × 2 mm), 400 × 400 × 111 (2 × 2 × 2 mm)
Scan duration	30 s, 60 s, 120 s, 300 s
FWHM	0, 2, 4, 6, 8 mm

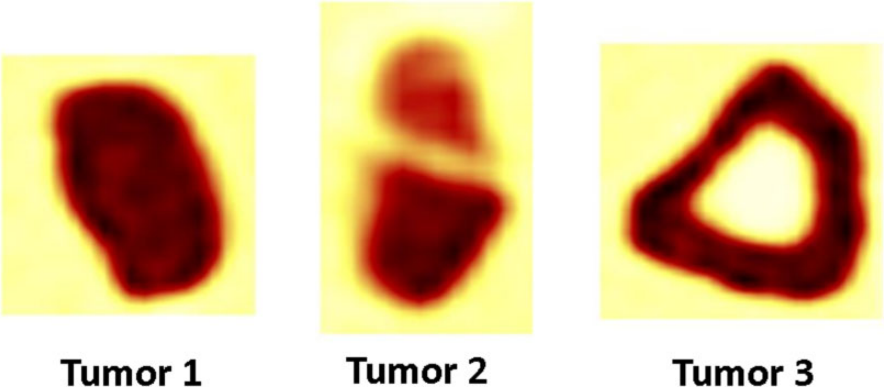

FIG. 1. PET images showing results with 3D printed inserts: tumor 1 with homogeneous uptake, tumor 2 with heterogeneity over 2 compartments, and tumor 3 containing a necrotic core (from left to right). [Color figure can be viewed at wileyonlinelibrary.com]

eventually resulted in an actual 3D VOI were considered for feature extraction (i.e., segmentations of 1 or 2 voxels or those located in a single image plane were discarded).

2.C. Radiomic feature extraction

Image processing and feature extraction were performed using Matlab 2014b. For each VOI, 246 radiomic features were calculated, including 19 morphological features, 3 local intensity features, 18 statistical features, and 206 textural features (100 gray level co-occurrence-based features, 64 gray level run length-based features, 32 gray level size zone-based features, and 10 neighborhood gray tone difference-based features).(18) All calculated features are listed in the supplemental materials (Table S1). Textural features were extracted from discretized image stacks that reduced the continuous-scaled SUV to a countable number of intensity values. Image stacks were discretized using a fixed number of 64 bins (FBN) and a fixed bin width (FBW) of 0.25 for the high uptake spheres and the 3D prints. For the low uptake spheres (SBR <1), a bin width of 0.05 was applied. Images were analyzed in both two and three dimensions with a connectivity of 8 and 26 voxels, respectively (using a Chebyshev norm of 1). Single feature values derived from the gray level co-occurrence and gray level run length matrices were calculated by both averaging the obtained feature values over all directions and by extracting the features directly from a single merged matrix in which the gray level co-occurrence or gray level run length matrices over all directions were summed. We ensured that image processing and feature calculation matched publicly available benchmark values of digital phantom and patient test data.[21]

2.D. Feature clustering

The number of radiomic features is usually high in comparison to the number of subjects included in a PET study. In order to avoid overfitting, the feature space has to be reduced before features can be used for classification or other purposes. In this study, clusters of features with the same properties were identified using a Spearman correlation matrix of the CT-segmented features, evaluating the monotonic relationship between features. The correlation matrix was ordered by minimizing the mean correlation difference between neighboring features. A cluster was defined by features that resulted in a high correlation, that is, that had mutual Spearman's correlation coefficients of >0.7.[22]

We have determined whether the composition of feature clusters was affected by discretization, reconstruction algorithm, sphere size, and activity uptake. For defining the correlation matrices, we used the default settings: all activity uptakes and sphere sizes, a European Association of Nuclear Medicine Research Ltd (EARL) compliant reconstruction (OSEM, 4 mm FWHM, 120 s scan duration),[23] matrix size 256 × 256 × 111, CT-based segmentation, and FBW discretization. The clusters of this default correlation matrix were compared with the clusters of other correlation matrices which were composed on the basis of different settings for discretization (FBW and FBN) and reconstruction (OSEM and PSF). Subsequently, the data of the default setting were divided into four subcategories: larger (diameters of 37, 28 and 22 mm) — high uptake spheres (SBR >1), larger — low uptake spheres (SBR <1), smaller (diameters of 17, 13 and 10 mm) — high uptake spheres, and smaller — low uptake spheres. In this case, all clusters were compared against the clusters of the default correlation matrix of the larger high uptake spheres. Moreover, we have compared the clusters of all statistically equal replicates using the default settings to ensure that all found differences in the composition of feature clusters could be ascribed to the sources of variation.

2.E. Repeatability analysis

Repeatability was evaluated using the intraclass correlation coefficient (ICC), calculated with the irr package (version 0.84), available from the Comprehensive R Archive Network (http://www.r-project.org). A two-way single measure model was used to evaluate the consistency of the replicates of each setting. The ICC is the ratio of the intercluster variance and the total variance, that is, the sum of the intracluster and intercluster variability. Intraclass correlation coefficient values lie between 0 and 1 representing perfect repeatability. Furthermore, a high ICC indicates a high intercluster variance in comparison with the intracluster variance. Therefore, features yielding a high ICC are also sensitive to insert-specific differences.

Before extracting the ICCs, the data were split into the same four different underlying data subcategories that were used for the redundancy analysis. The 3D inserts are forming an additional subcategory. The ICC was calculated for every combination of subcategory, matrix size, reconstruction algorithm, scan duration, Gaussian filter, discretization method, and segmentation method. Each sphere with a different size or SBR, as well as each 3D insert, was considered a different subject. The equivalent replicates were regarded as the different raters. Features exhibiting an ICC >0.8 were considered to represent good repeatability.[24] For each setting, the percentage of repeatable features was obtained to identify trends in the data. Smaller subsets of features were analyzed in order to avoid that large groups of features with similar properties overrepresented and biased the analysis. For this purpose, we used a predefined set of uncorrelated radiomic features, as identified previously (Table II, Supplemental Figures S1–S4).[9]

To investigate the potential relationship between the repeatability of radiomic features and image noise, a variance image of the statistically equal replicates was calculated for every studied setting. The image noise was measured by calculating the coefficient of variation over four different spherical VOIs defined in the phantom background of the variance image.

TABLE II. Predefined feature set used for repeatability analysis shown in Supplemental Figures S1–S4.

Selection of uncorrelated features
Homogeneity$_{3D}$ (NGLDM)
Energy
Short runs emphasis$_{3D}$
Gray level nonuniformity$_{3D}$
Skewness
Long zone low gray level emphasis$_{3D}$
Long run emphasis$_{3D}$
Low gray level run emphasis$_{3D}$
High gray level run emphasis$_{3D}$
SUVmax
Busyness

3. RESULTS

3.A. Feature clustering

Figures 2 and 3 demonstrate how the Spearman's correlation matrix was affected by reconstruction algorithm and discretization method (Fig. 2), as well as by sphere size and activity uptake (Fig. 3). In order to illustrate the differences in correlation, the feature order and cluster composition of the default setting were used to display the correlation matrices of the other settings. The correlation matrix of this setting is displayed in the upper left corner of each figure. Changing the reconstruction algorithm to PSF had a minor impact on the correlation matrix. However, the increased number of clusters being composed of features with mutual Spearman's correlation coefficients of <0.7 demonstrates that the impact of the discretization method was much larger. Similarly, Fig. 2 shows that sphere size and activity uptake both had a

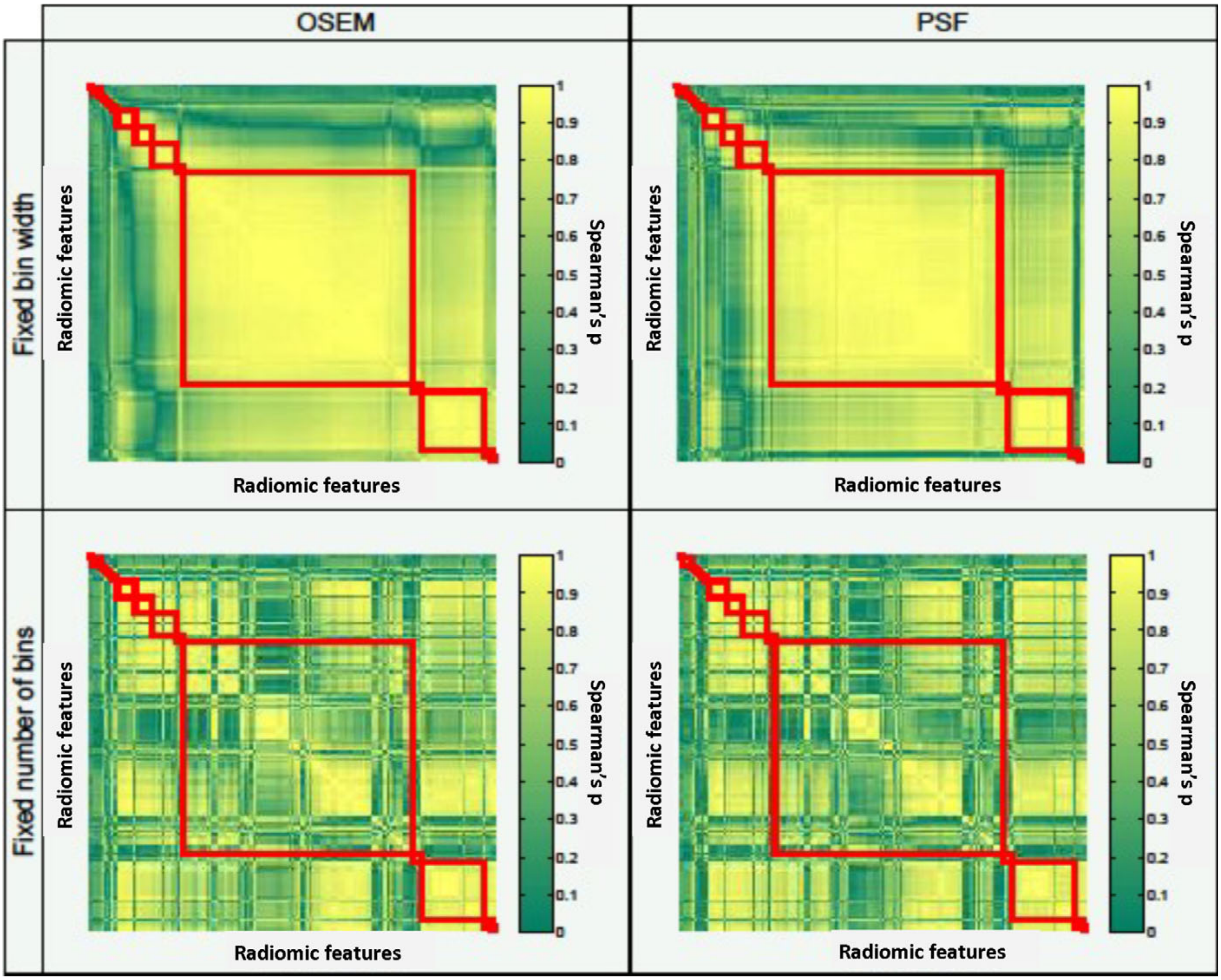

FIG. 2. Impact of discretization and reconstruction setting on the composition of feature clusters: feature clusters (red rectangles) were defined based on Spearman's correlation matrices. The default setting in the upper left corner consists of all activity uptakes and sphere sizes, matrix size 256 × 256 × 111, OSEM reconstruction, 120 s scan duration, FBW discretization, 4 mm FWHM, and CT-based segmentation. The feature order of this setting was also used to display the correlation matrices of the other settings. [Color figure can be viewed at wileyonlinelibrary.com]

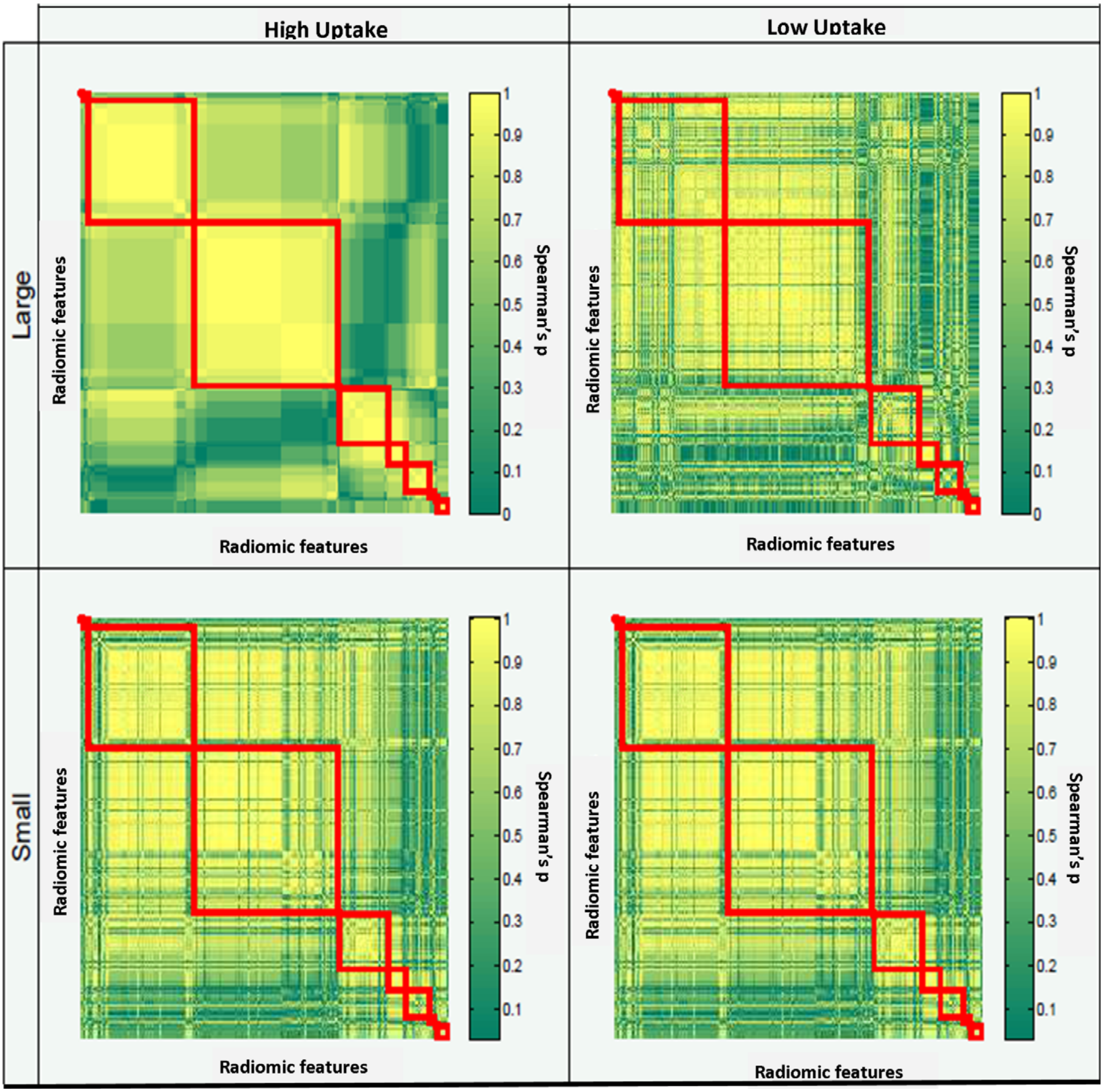

FIG. 3. Impact of sphere size and activity uptake on the composition of feature clusters: feature clusters (red rectangles) were defined based on Spearman's correlation matrices. The default setting in the upper left corner consists of the data of larger high uptake spheres, EARL reconstruction, matrix size 256 × 256 × 111, 120 s scan duration, FBW discretization, and CT-based segmentation. The feature order of this setting was also used to display the correlation matrices of the other settings. [Color figure can be viewed at wileyonlinelibrary.com]

major impact on the correlation matrix. The correlation matrices of the statistically equal replicates showed to be similar, and therefore all found differences in the composition of feature clusters could be ascribed to the sources of variation.

3.B. Repeatability analysis

Repeatability analysis was not performed for 15 geometry features derived from the CT-based segmentation, as they are a function of sphere size and hence exhibit an ICC of 1 by definition. The ICC values of every calculated feature for discretization with FBW and FBN are listed in the supplemental material (Tables S1 and S2). Figures 4 and 5 display how the repeatability of radiomic features is affected by heterogeneity, activity uptake, sphere size, discretization method, image noise, reconstruction algorithm, and matrix/voxel size for CT-based segmentations. The impact of the same sources of

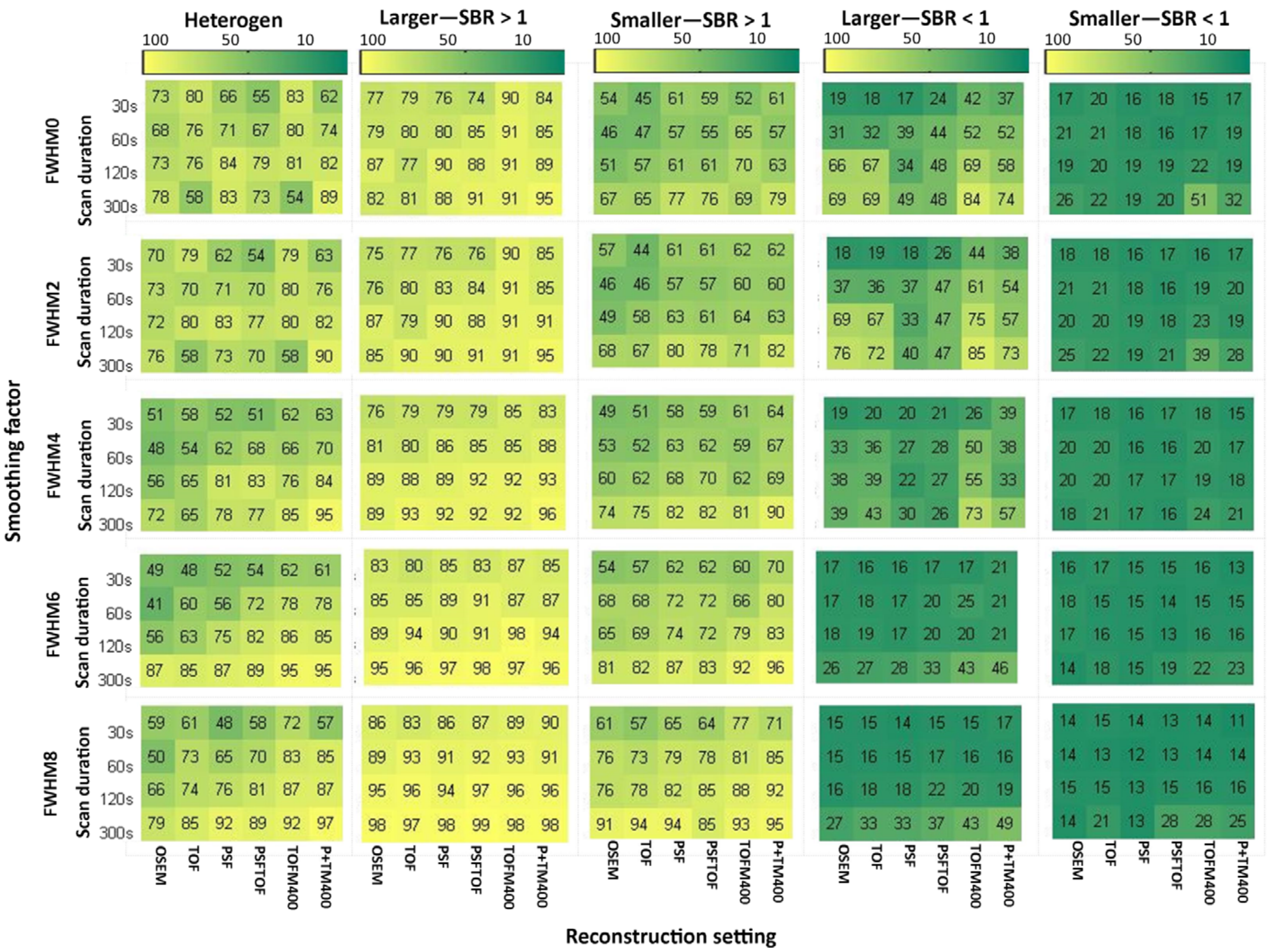

FIG. 4. Percentage of repeatable features discretized with FBW: Percentage of all features discretized with FBW and segmented based on CT exhibiting an ICC >0.8 for all studied settings and underlying data categories (from left to right: heterogeneous 3D prints, bigger spheres with high uptake, smaller spheres with high uptake, bigger spheres with low uptake, and smaller spheres with low uptake). TOFM400/P+TM400: TOF/PSF+TOF reconstruction with matrix size 400 × 400. [Color figure can be viewed at wileyonlinelibrary.com]

variation for PET-based segmentations is displayed in Figs. 6 and 7.

In general, underlying data, image noise, and discretization method had a high impact on feature repeatability. The reconstruction setting had also a big influence, when FBN discretization was applied. Regarding the underlying data, bigger spheres yielded more repeatable features than smaller spheres and spheres with high activity uptake yielded more repeatable features than spheres with low activity uptake. In terms of repeatability, 3D printed inserts showed comparable results with those of larger high uptake spheres. Image noise reduction in terms of longer scan durations and applying smoothing to the images resulted in better repeatability, although the effects of smoothing depended on the segmentation and discretization method. The inverse proportional relationship between number of repeatable features and noise is illustrated in Fig. 8. This figure shows the number of repeatable features discretized with FBN for the NEMA IQ phantom scan with SBR 1:10 for all reconstruction methods, scan durations, smoothing factors, and matrix sizes as function of noise. The impact of image noise depended on the used discretization method: For FBN discretization (Figs. 5 and 7), the number of repeatable features increased with applied smoothing. For FBW discretization of high uptake spheres and 3D prints, the effect of smoothing was marginal (Figs. 4 and 6), while for low uptake spheres, an increase in smoothing even led to less repeatable features. In particular when FBN and PET-based segmentations are used in combination, mitigation of noise by smoothing seems to be beneficial in terms of more repeatable features, while for FBW and CT-based segmentation smoothing as means of noise reduction seems less effective. Both discretization methods yielded in general different repeatability pattern: FBW discretization led to better repeatability and to less variation across reconstruction algorithms. While for FBN discretization, differences across reconstruction algorithm were mainly observed for longer (120 and 300 s) scan durations. For those scan durations, the repeatability was the lowest for images reconstructed with OSEM or TOF and increased by adding PSF.

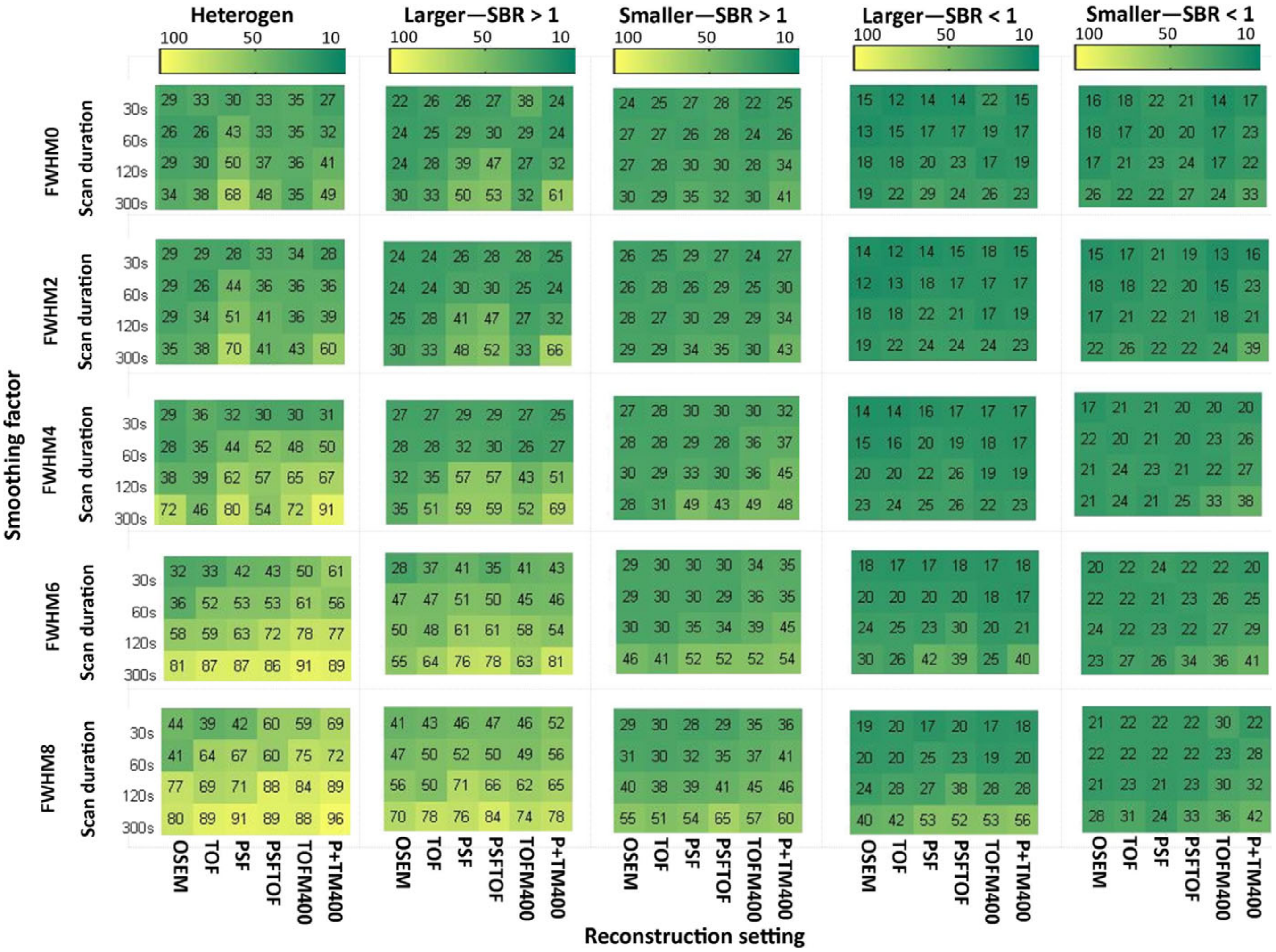

Smoothing factor	Scan duration	Heterogen OSEM	TOF	PSF	PSFTOF	TOFM400	P+TM400
FWHM0	30s	29	33	30	33	35	27
	60s	26	26	43	33	35	32
	120s	29	30	50	37	36	41
	300s	34	38	68	48	35	49
FWHM2	30s	29	29	28	33	34	28
	60s	29	26	44	36	36	36
	120s	29	34	51	41	36	39
	300s	35	38	70	41	43	60
FWHM4	30s	29	36	32	30	30	31
	60s	28	35	44	52	48	50
	120s	38	39	62	57	65	67
	300s	72	46	80	54	72	91
FWHM6	30s	32	33	42	43	50	61
	60s	36	52	53	53	61	56
	120s	58	59	63	72	78	77
	300s	81	87	87	86	91	89
FWHM8	30s	44	39	42	60	59	69
	60s	41	64	67	60	75	72
	120s	77	69	71	88	84	89
	300s	80	89	91	89	88	96

Smoothing factor	Scan duration	Larger—SBR > 1 OSEM	TOF	PSF	PSFTOF	TOFM400	P+TM400
FWHM0	30s	22	26	26	27	38	24
	60s	24	25	29	30	29	24
	120s	24	28	39	47	27	32
	300s	30	33	50	53	32	61
FWHM2	30s	24	24	26	28	28	25
	60s	24	24	30	30	25	24
	120s	25	28	41	47	27	32
	300s	30	33	48	52	33	66
FWHM4	30s	27	27	29	29	27	25
	60s	28	28	32	30	26	27
	120s	32	35	57	57	43	51
	300s	35	51	59	59	52	69
FWHM6	30s	28	37	41	35	41	43
	60s	47	47	51	50	45	46
	120s	50	48	61	61	58	54
	300s	55	64	76	78	63	81
FWHM8	30s	41	43	46	47	46	52
	60s	47	50	52	50	49	56
	120s	56	50	71	66	62	65
	300s	70	78	76	84	74	78

Smoothing factor	Scan duration	Smaller—SBR > 1 OSEM	TOF	PSF	PSFTOF	TOFM400	P+TM400
FWHM0	30s	24	25	27	28	22	25
	60s	27	27	26	28	24	26
	120s	27	28	30	30	28	34
	300s	30	29	35	32	30	41
FWHM2	30s	26	25	29	27	24	27
	60s	26	28	26	29	25	30
	120s	28	27	30	29	29	34
	300s	29	29	34	35	30	43
FWHM4	30s	27	28	30	30	30	32
	60s	28	28	29	28	36	37
	120s	30	29	33	30	36	45
	300s	28	31	49	43	49	48
FWHM6	30s	29	30	30	30	34	35
	60s	29	30	30	29	36	35
	120s	30	30	35	34	39	45
	300s	46	41	52	52	52	54
FWHM8	30s	29	30	28	29	35	36
	60s	31	30	32	35	37	41
	120s	40	38	39	41	45	46
	300s	55	51	54	65	57	60

Smoothing factor	Scan duration	Larger—SBR < 1 OSEM	TOF	PSF	PSFTOF	TOFM400	P+TM400
FWHM0	30s	15	12	14	14	22	15
	60s	13	15	17	17	19	17
	120s	18	18	20	23	17	19
	300s	19	22	29	24	26	23
FWHM2	30s	14	12	14	15	18	15
	60s	12	13	18	17	17	17
	120s	18	18	22	21	17	19
	300s	19	22	24	24	24	23
FWHM4	30s	14	14	16	17	17	17
	60s	15	16	20	19	18	17
	120s	20	20	22	26	19	19
	300s	23	24	25	26	22	23
FWHM6	30s	18	17	17	18	17	18
	60s	20	20	20	20	18	17
	120s	24	25	23	30	20	21
	300s	30	26	42	39	25	40
FWHM8	30s	19	20	17	20	17	18
	60s	20	20	25	23	19	20
	120s	24	28	27	38	28	28
	300s	40	42	53	52	53	56

Smoothing factor	Scan duration	Smaller—SBR < 1 OSEM	TOF	PSF	PSFTOF	TOFM400	P+TM400
FWHM0	30s	16	18	22	21	14	17
	60s	18	17	20	20	17	23
	120s	17	21	23	24	17	22
	300s	26	22	22	27	24	33
FWHM2	30s	15	17	21	19	13	16
	60s	18	18	22	20	15	23
	120s	17	21	22	21	18	21
	300s	22	26	22	22	24	39
FWHM4	30s	17	21	21	20	20	20
	60s	22	20	21	20	23	26
	120s	21	24	23	21	22	27
	300s	21	24	21	25	33	38
FWHM6	30s	20	22	24	22	22	20
	60s	22	22	21	23	26	25
	120s	24	22	23	22	27	29
	300s	23	27	26	34	36	41
FWHM8	30s	21	22	22	22	30	22
	60s	22	22	22	22	23	28
	120s	21	23	21	23	30	32
	300s	28	31	24	33	36	42

FIG. 5. Percentage of all features discretized with FBN: Percentage of all features discretized with FBN and segmented based on CT exhibiting an ICC >0.8 for all studied settings and underlying data categories (from left to right: heterogeneous 3D prints, bigger spheres with high uptake, smaller spheres with high uptake, bigger spheres with low uptake, and smaller spheres with low uptake). TOFM400/P+TM400: TOF/PSF+TOF reconstruction with matrix size 400 × 400. [Color figure can be viewed at wileyonlinelibrary.com]

On the other hand, the used matrix size as well as the segmentation method had only minor impact on repeatability: Changes in matrix size led mainly to differences for the heterogeneous inserts and the low uptake spheres, where a bigger matrix size (i.e., a smaller voxel size) resulted in more repeatable features. Also differences between segmentation methods were mainly observed for the low uptake data. For the smaller low uptake spheres and PET-based segmentations, the number of repeatable features was lower than for CT-based segmentations and decreased even more with increasing smoothing. An overview of the parameters leading to the best repeatability behavior for the different activity uptake groups is listed in Table III.

3.C. Repeatable features

Repeatable features for all subcategories and the EARL-compliant reconstruction are listed in Table IV for both discretization methods. Even though every subcategory resulted in more repeatable features for FBW discretization, the number of features found to be repeatable for all subcategories is comparable for both discretization methods with a big overlap: Five features were found to be repeatable only for FBW discretization, two only for FBN discretization, sixteen features for both methods, and two features do not require the discretization step.

4. DISCUSSION

This study demonstrated that both dimensionality reduction and repeatability of ^{18}F-FDG PET radiomic features are sensitive to most sources of variation. In the subsequent sections, the underlying trends are described in more detail.

4.A. Feature clustering

As described in several other studies,[9,25] we found that many features were highly correlated. Discretization, sphere size, and activity uptake had a major impact on this correlation, while reconstruction method had less influence. To

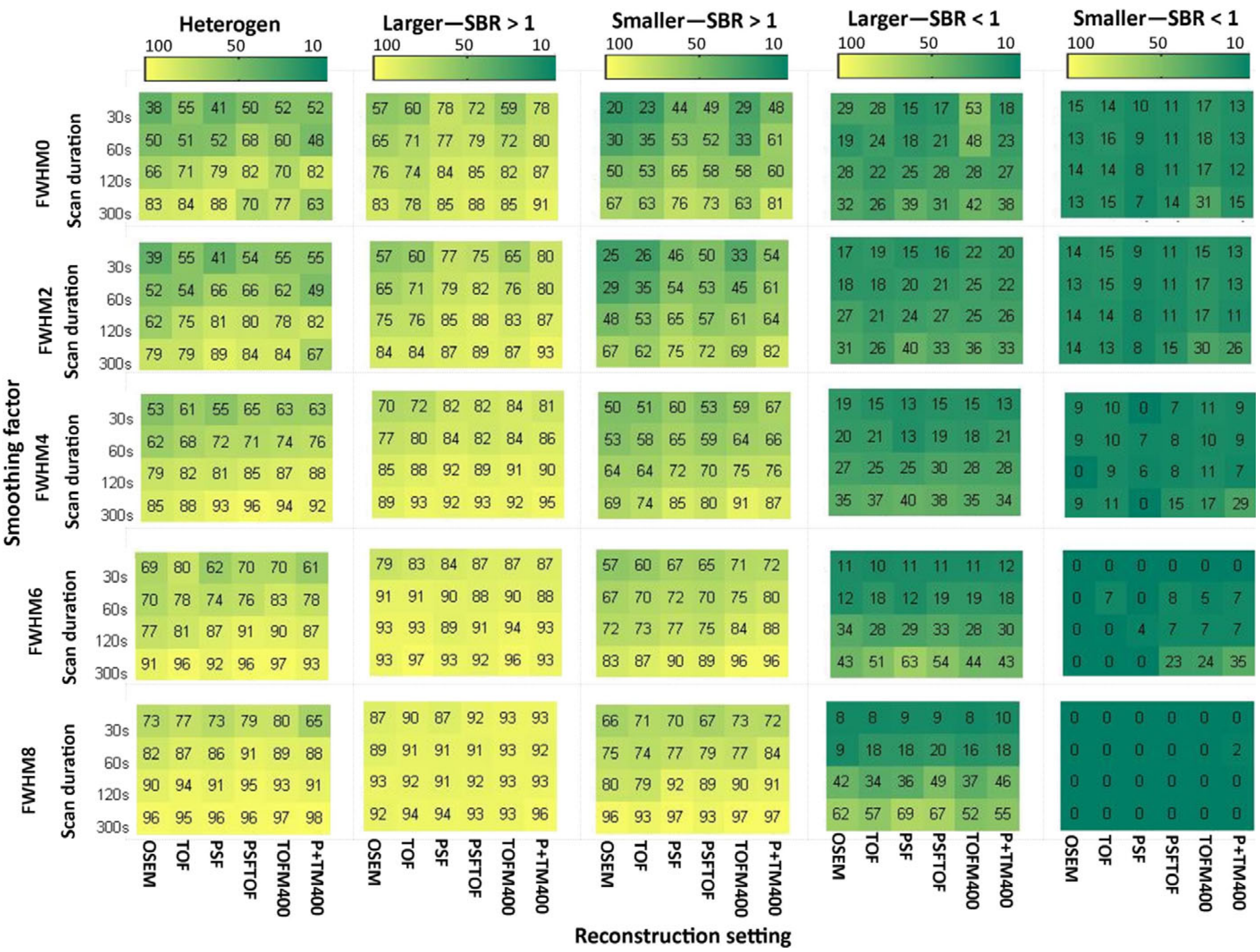

FIG. 6. Percentage of repeatable features discretized with FBW: Percentage of all features discretized with FBW and segmented based on PET exhibiting an ICC >0.8 for all studied settings and underlying data categories (from left to right: heterogeneous 3D prints, bigger spheres with high uptake, smaller spheres with high uptake, bigger spheres with low uptake, and smaller spheres with low uptake). TOFM400/P+TM400: TOF/PSF+TOF reconstruction with matrix size 400 × 400. [Color figure can be viewed at wileyonlinelibrary.com]

reduce the feature space, representative features should be chosen from each cluster. We showed that the composition of the correlation matrices was repeatable, but dependent on various factors such as image discretization, activity uptake, and sphere size. As a consequence, these correlation matrices yield different clusters of correlated features. Therefore, the representative features extracted from these clusters will differ across these matrices. Hence, the outcome of redundancy analyses is only generalizable among studies when these studies applied similar settings.

4.B. Feature repeatability

In this study, radiomic features extracted from larger high uptake spheres (SBR >1) generally showed higher repeatability than those extracted from smaller low uptake spheres (SBR <1). In a clinical setting, the tracer uptake activity is affected by tumor type and uptake mechanism. Furthermore, the signal depends on the used PET isotope. This can result in images with a poor signal-to-noise ratio (e.g., ^{89}Zr-antibodies in immunoPET studies) or even in very low uptake areas (lower than surrounding background). Therefore, it is not recommended to generalize results of radiomic studies in different tumor types and PET tracers, as most studies so far explored the performance of radiomic features on FDG PET/CT studies.

In radiomic studies, both discretization methods (FBW as well as FBN) are widely used. However, several studies suggest the use of FBW discretization as better clinical applicability and repeatability has been shown.[21,26,27] Furthermore, Orlhac et al. demonstrated that features discretized with FBW led to more significant differences in feature values across tumor types and hence to more meaningful results.[19] Our findings also support the use of FBW discretization, as it led in general to a larger number of repeatable features (yielding a high ICC) for both phantoms and hence also to more features sensitive to heterogeneity information.

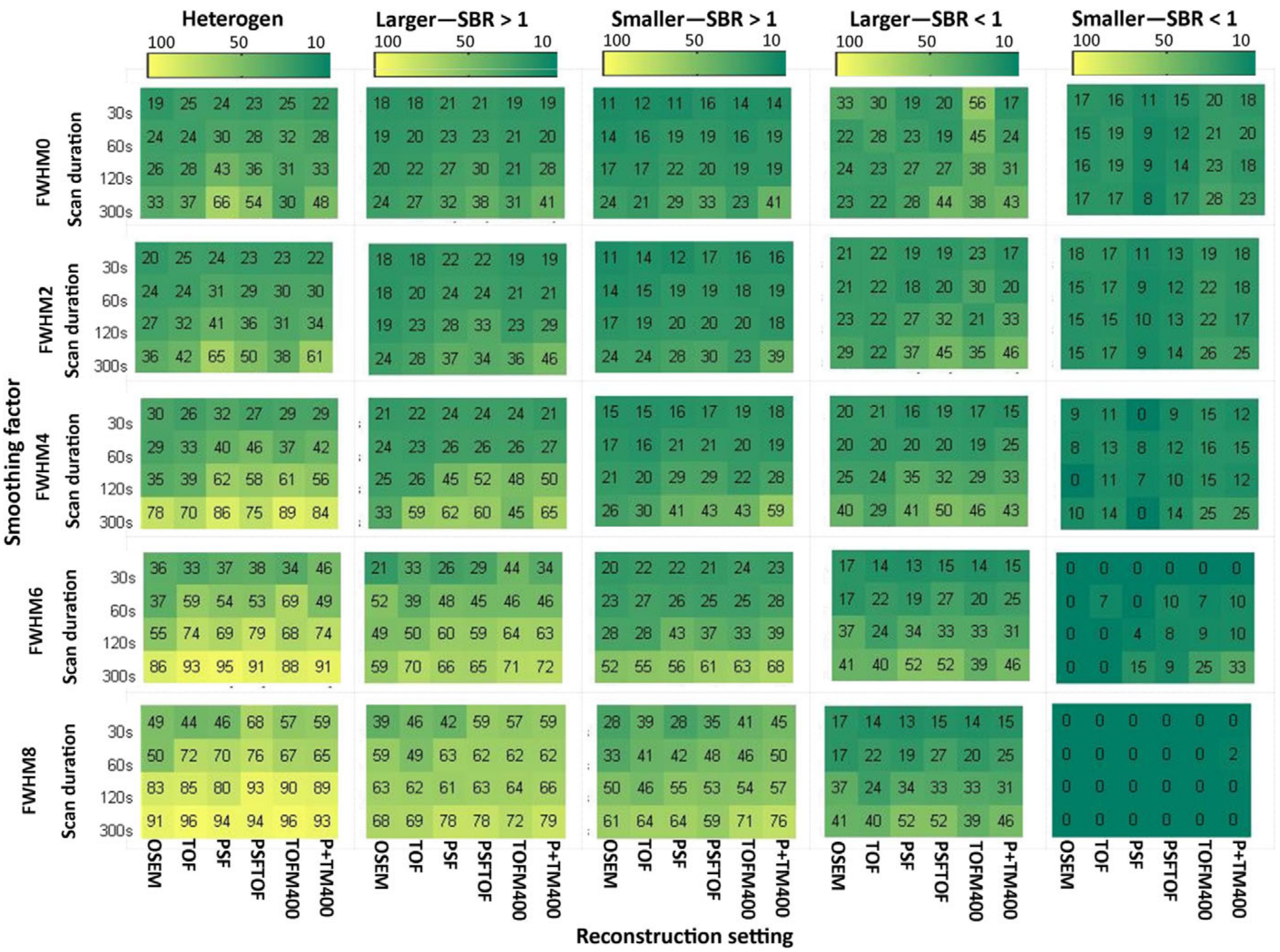

FIG. 7. Percentage of repeatable features discretized with FBN: Percentage of all features discretized with FBW and segmented based on PET exhibiting an ICC >0.8 for all studied settings and underlying data categories (from left to right: heterogeneous 3D prints, bigger spheres with high uptake, smaller spheres with high uptake, bigger spheres with low uptake, and smaller spheres with low uptake). TOFM400/P+TM400: TOF/PSF+TOF reconstruction with matrix size 400 × 400. [Color figure can be viewed at wileyonlinelibrary.com]

Previous studies reported high variability of feature values across reconstruction algorithm[11,14] for images discretized with FBN. Our results confirm that FBN discretization led also to higher variation in repeatability performance across reconstruction algorithm. A reason for this effect might be that for this setting, the bin width is sensitive to image noise and therefore every image is discretized with a different bin width. This hypothesis is in line with the finding that decreasing image noise by image smoothing resulted in increased number of repeatable features mostly for FBN discretization. Another point that supports this hypothesis is that also the combination of FBN discretization and PET-based segmentation resulted in an increase in number of repeatable features, when compared with CT-segmentation. This is likely due to the fact that the 41% SUV_{peak} method eliminates outliers from the region of interest. Therefore, the intensity ranges across regions of interests (and also the bin width) become comparable across images and lead therefore to an increase in repeatability.

Our results suggest that a large number of features are sensitive to image noise. In the majority of the cases, increased smoothing resulted in a higher number of repeatable features (Figs. 4 and 5), and these effects are most pronounced when using PET-based segmentation in combination with FBN discretization (Fig. 7). This may seem counter-intuitive as for smoothing there is a trade-off between noise and spatial resolution; that is, increased smoothing leads to less noise but lower spatial resolution and possibly less observable uptake heterogeneity. PET textural features, capturing intensity differences between neighboring voxels, can be highly sensitive to stochastic image variation.[12] As the reduction of noise leads to more homogeneous image texture, this may lead to more comparable textural matrices across the statistically equal replicates and hence to higher repeatability. A drawback of decreasing image noise by image smoothing might be that important textural information describing tumor uptake heterogeneity might get lost. In our study, however, for high uptake data and 3D printed heterogeneous inserts, actually more features showed good repeatability with

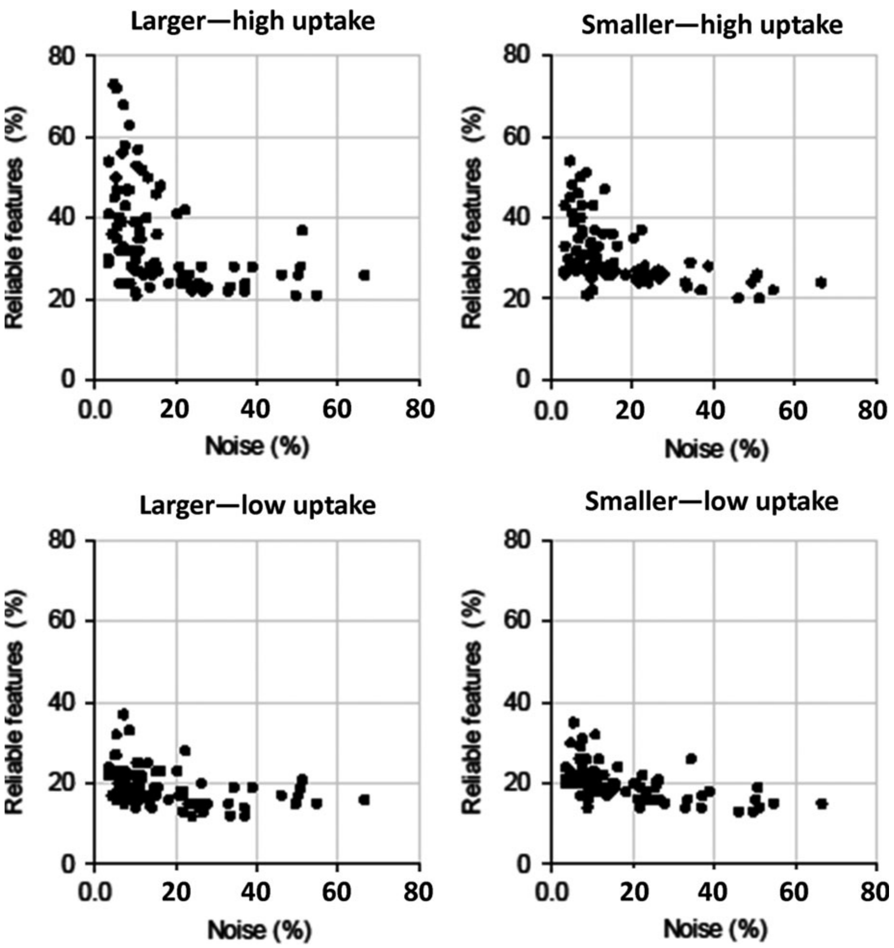

Fig. 8. Influence of noise on number of repeatable features extracted from NEMA IQ phantom scan with SBR 1:10 for all reconstructions, scan durations, smoothing factors, and matrix sizes: Number of repeatable features in the different subcategories as function of image noise

increasing smoothing and/or for longer scan duration. This indicates that for the heterogeneous phantom insert data, increasing smoothing did not necessarily eliminate important heterogeneity information. Therefore, noise mitigation by increasing scan statistics and/or by image smoothing could be a valid option and should be further explored. As the 3D printed inserts contain only coarse heterogeneity information, these findings can only be applied to tumors showing similar heterogeneity pattern as the 3D printed inserts. For tumors showing subtle heterogeneity uptake, smoothing might affect the heterogeneity information and therefore also influence the repeatability behavior of radiomic features. Furthermore, in this study, it was impossible to assess the impact of smoothing on the sensitivity of feature values to underlying biological factors.

On the other hand, low uptake spheres (SBR <1) discretized with FBW resulted in lower repeatability for higher levels of smoothing. In this case, smoothing decreased the intensity range in the spheres and therefore the chosen bin width can become inappropriate. Therefore, for low activity uptake, the bin width should be chosen carefully and/or the use of smoothing should be applied with care and/or avoided all together.

Several studies showed that a large number of features exhibit high variability across various reconstruction settings.[13,15,28] Our study showed that especially for FBN discretization the number of repeatable features also depended on the used reconstruction algorithm. For example, images reconstructed with PSF or PSF + TOF yielded higher repeatability than OSEM or TOF reconstructions. The higher repeatability found by using PSF is consistent with the fact that PSF decreases image noise[29] and with the previously reported finding that image noise and repeatability have an inverse proportional relationship. Moreover, the additional use of TOF improves image quality and reduces image noise[30] and is therefore expected to increase feature repeatability. However, our results showed the same repeatability for images reconstructed with OSEM and images reconstructed with TOF. A comparison of image noise between these images showed that the TOF-effect on our scanner and for this phantom was small and had therefore also only a small effect on the repeatability of features.

Many studies reported on differences in feature values across different voxel sizes.[31,32] In our study, differences in repeatability were mainly observed for the tumor-like inserts. Here, a smaller voxel size resulted in more repeatable

TABLE III. Parameters/methods/settings leading to best repeatability for different activity uptake groups.

	Heterogeneous inserts	High uptake spheres	Low uptake spheres
Reconstruction	Minor impact	Minor impact	PSF+TOF
Matrix/voxel size	Minor impact	Minor impact	Smaller voxel size (2 × 2 × 2 mm)
Scan duration	300 s	300 s	300 s
Smoothing (FWHM)	6/8 mm	6/8 mm	0 mm
Discretization method	FBW (bin width 0.25)	FBW (bin width 0.25)	FBW (bin width 0.05)
Segmentation method	Minor impact	Minor impact	CT-based segmentation

TABLE IV. Features with an ICC >0.8 for all subcategories and EARL-compliant reconstruction for both discretization methods

FBN	FBW
Integrated intensity (does not require discr.)	Integrated intensity (does not require discr.)
Energy intensity (does not require discr.)	Energy intensity (does not require discr.)
Joint-maximum$_{\text{2D\_avg}}$	Joint-maximum$_{\text{2D\_avg}}$
Joint-entropy$_{\text{2D\_avg}}$	Joint-entropy$_{\text{2D\_avg}}$
Difference-entropy$_{\text{2D\_avg}}$	Difference-entropy$_{\text{2D\_avg}}$
Sum-entropy$_{\text{2D\_avg}}$	Sum-entropy$_{\text{2D\_avg}}$
Angular-second-moment$_{\text{2D\_avg}}$	Angular-second-moment$_{\text{2D\_avg}}$
Joint-entropy$_{\text{2D\_comb}}$	Joint-entropy$_{\text{2D\_comb}}$
First measure of information correlation$_{\text{3D\_avg}}$	
	Gray level nonuniformity GLRLM$_{\text{2D\_avg}}$
Run length nonuniformity$_{\text{2D\_avg}}$	Run length nonuniformity$_{\text{2D\_avg}}$
Run-entropy$_{\text{2D\_avg}}$	Run-entropy$_{\text{2D\_avg}}$
	Gray level nonuniformity GLRLM$_{\text{2D\_comb}}$
Run length nonuniformity$_{\text{2D\_comb}}$	Run length nonuniformity$_{\text{2D\_comb}}$
Run entropy$_{\text{2D\_comb}}$	Run entropy$_{\text{2D\_comb}}$
Gray level nonuniformity GLRLM$_{\text{3D\_avg}}$	Gray level nonuniformity GLRLM$_{\text{3D\_avg}}$
Run length nonuniformity$_{\text{3D\_avg}}$	Run length nonuniformity$_{\text{3D\_avg}}$
Gray level nonuniformity GLRLM$_{\text{3D\_comb}}$	Gray level nonuniformity GLRLM$_{\text{3D\_comb}}$
Run length nonuniformity$_{\text{3D\_comb}}$	Run length nonuniformity$_{\text{3D\_comb}}$
	Gray level nonuniformity normalized GLSZM$_{\text{2D}}$
Zone size nonuniformity$_{\text{2D}}$	Zone size nonuniformity$_{\text{2D}}$
Zone size entropy$_{\text{2D}}$	Zone size entropy$_{\text{2D}}$
Zone size nonuniformity$_{\text{3D}}$	
	Gray level nonuniformity GLSZM$_{\text{3D}}$
	Coarseness$_{\text{3D}}$

features. A possible explanation might be that the smaller voxel size can capture heterogeneity information more precisely and it is therefore preferable to follow the recent recommendation by Hatt et al. to apply a standardized voxel size of 2 × 2 × 2 mm[8]. The latter is also recommended because the value of some features depends on the number of voxels within a given VOI.

Previous studies reported a high variability of feature values across different segmentation results.[27,28,33,34] However, as demonstrated by Hatt et al.[33] even though different segmentations lead to a variability in feature values, their predictive value might not change. Our results indicate that the 41% SUV$_{\text{peak}}$ segmentation algorithm leads to good repeatability for a large number of features in line with,[34] although it does not lead to reliable segmentations in all cases.[35] In our study, differences in repeatability were mainly observed in the low uptake data. As explained before, for PET-segmentations, image noise influences not only the repeatability of radiomic features but also the quality of the segmentation. Therefore, the lower number of repeatable features in the low uptake data might be caused by poor segmentation results due to image noise.

4.C. Repeatable features

Only a small number of features were identified to be repeatable for all subcategories. The majority of these features were repeatable for both discretization methods. Some of these features (gray level nonuniformity run length, run length nonuniformity) were identified before to be insensitive to the discretization step.[9] The high ICC also indicates that these features are informative regarding differences in tracer uptake heterogeneity. This is in line with previous studies showing that, for example, coarseness contains valuable information about survival for NSCLC patients or response to therapy for esophageal cancer patients.[36,37] While sum and difference entropy (GLCM) showed to have prognostic value for NSCLC tumors.[38–40]

A drawback of our study is that only phantom data were included, although we attempted to make the study as clinically relevant as possible by using 3D printed phantom inserts reflecting heterogeneous tumor uptake pattern. It should be noted that our study was designed to explore the technical performance of radiomic features under controlled experimental conditions, thereby avoiding biological uncertainties or variations in imaging procedures. Yet, it is of interest to perform, for example, repeatability studies which include these factors to further test radiomic performance under clinical conditions. Our results show that it may be warranted to collect these repeatability studies for various diseases and tracers as the tracer bio distribution and tumor uptake can be very different among patient groups and tracers. We showed that differences in size, level, and intratumoral distribution of tracer uptake have a large effect on radiomic feature repeatability and thus on the optimal settings to be used in a radiomics analysis pipeline.

5. CONCLUSION

This study reports on the impact of underlying data, image reconstruction methods and settings, noise, discretization method, and delineation method on the dimensionality reduction and repeatability of ^{18}F-FDG PET radiomic features, which is an important measurement of error. Our data show that feature reduction is sensitive to discretization, sphere size, and activity uptake, and is therefore only generalizable among studies using the same settings. This study demonstrates that clinical PET studies and examinations need to be standardized in order to use ^{18}F-FDG PET radiomics as quantitative imaging biomarkers. Although this conclusion is not new for standard quantitative PET biomarkers, our study suggests that, in particular for radiomics features, efforts should focus on noise reduction sometimes even at the cost of spatial resolution and optimizing the choice for image reconstruction method, discretization method, and segmentation method. For every clinical application, radiotracer and disease type, a validation of radiomic feature performance/repeatability needs to be performed as its performance depends on the nature of the underlying data, that is, as function of tumor size, shape, tracer uptake level, contrast, and intratumoral uptake distribution.

ACKNOWLEDGMENTS

This work is part of the research program STRaTeGy with project number 14929, which was (partly) financed by the Netherlands Organisation for Scientific Research (NWO). This work was (in part) financially supported by the Netherlands Organisation for Health Research and Development (grant 10-10400-98-14002). This study was financed by the Dutch Cancer Society, POINTING project, grant 10034.

CONFLICTS OF INTEREST

The authors have no relevant conflicts of interest to disclose.

[*] These authors have equally contributed to this work and are in control over the presented data.

[a] Author to whom correspondence should be addressed. Electronic mail: e.a.g.pfaehler@umcg.nl; Telephone: (+31) 503613471; Fax: (+31) 5036.

REFERENCES

1. Zhang Y, Oikonomou A, Wong A, Haider MA, Khalvati F. Radiomics-based prognosis analysis for non-small cell lung cancer. *Sci Rep*. 2017;7:46349.
2. Huang W, Fan M, Liu B, et al. Value of metabolic tumor volume on repeated ^{18}F-FDG PET/CT for early prediction of survival in locally advanced non-small cell lung cancer treated with concurrent chemoradiotherapy. *J Nucl Med*. 2014;55:1584–1590.
3. Hatt M, Majdoub M, Vallieres M, et al. ^{18}F-FDG PET uptake characterization through texture analysis: investigating the complementary nature of heterogeneity and functional tumor volume in a multi-cancer site patient cohort. *J Nucl Med*. 2015;56:38–44.
4. O'Connor JPB, Rose CJ, Waterton JC, Carano RAD, Parker GJM, Jackson A. Imaging intratumor heterogeneity: role in therapy response, resistance, and clinical outcome. *Clin Cancer Res*. 2015;21:249–257.
5. Zhang Y, Oikonomou A, Wong A, Haider MA, Khalvati F. Radiomics-based prognosis analysis for non-small cell lung cancer. *Sci Rep*. 2017;7:46349.
6. Aerts HJWL, Velazquez ER, Leijenaar RTH, et al. Decoding tumour phenotype by noninvasive imaging using a quantitative radiomics approach. *Nat Commun*. 2014;5:4006.
7. Vallières M, Freeman CR, Skamene SR, El Naqa I. A radiomics model from joint FDG-PET and MRI texture features for the prediction of lung metastases in soft-tissue sarcomas of the extremities. *Phys Med Biol*. 2015;60:5471–5496.
8. Hatt M, Tixier F, Pierce L, et al. Characterization of PET/CT images using texture analysis: the past, the present . . . any future ? *Eur J Nucl Med Mol Imaging*. 2017;44:151–165.
9. Orlhac F, Soussan M, Maisonobe J, Garcia CA, Vanderlinden B, Buvat I. Tumor texture analysis in ^{18}F-FDG PET: relationships between texture parameters, histogram indices, standardized uptake values, metabolic volumes, and total lesion glycolysis. *J Nucl Med*. 2014;55:414–422.
10. Kumar V, Gu Y, Basu S, et al. Radiomics: the process and the challenges. *Magn Reson Imaging*. 2012;30:1234–1248.
11. Cortes-Rodicio J, Sanchez-Merino G, Garcia-Fidalgo MA, Tobalina-Larrea I. Identification of low variability textural features for heterogeneity quantification of ^{18}F-FDG PET/CT imaging, Rev. *Española Med Nucl Imagen Mol (English Ed)*. 2016;35:379–384.
12. Nyflot MJ, Yang F, Byrd D, Bowen SR, Sandison GA, Kinahan PE. Quantitative radiomics: impact of stochastic effects on textural feature analysis implies the need for standards. *J Med Imaging*. 2015;2:041002.
13. Galavis PR, Hollensen C, Jallow N, Paliwal B, Jeraj R. Variability of textural features in FDG PET images due to different acquisition modes and reconstruction parameters. *Acta Oncol*. 2014;49:1012–1016.
14. Yan J, Chu-Shern JL, Loi HY, et al. Impact of image reconstruction settings on texture Features in ^{18}F-FDG PET. *J Nucl Med*. 2015;56:1667–1673.
15. Shiri I, Rahmim A, Ghaffarian P, Geramifar P, Abdollahi H, Bitarafan-Rajabi A. The impact of image reconstruction settings on ^{18}F-FDG PET radiomic features: multi-scanner phantom and patient studies. *Eur Radiol*. 2017;27:4498–4509.
16. Bailly C, Bodet-Milin C, Couespel S, et al. Revisiting the robustness of PET-based textural features in the context of multi-centric trials. *PLoS ONE*. 2016;11:e0159984.
17. Belli ML, Mori M, Broggi S, et al. Quantifying the robustness of [18 F] FDG-PET/CT radiomic features with respect to tumor delineation in head and neck and pancreatic cancer patients. *Phys Medica*. 2018;49:105–111.
18. Desseroit M-C, Tixier F, Weber WA, et al. Reliability of PET/CT shape and heterogeneity features in functional and morphologic components of non-small cell lung cancer tumors: a repeatability analysis in a prospective multicenter cohort. *J Nucl Med*. 2017;58:406–411.
19. Orlhac F, Soussan M, Chouahnia K, Martinod E, Buvat I. ^{18}F-FDG PET-derived textural indices reflect tissue-specific uptake pattern in non-small cell lung cancer. *PLoS ONE*. 2015;10:e0145063.
20. Boellaard R, Delgado-Bolton R, Oyen WJG, et al. FDG PET/CT: EANM procedure guidelines for tumour imaging: version 2.0. *Eur J Nucl Med Mol Imaging* 2015;42:328–354.
21. Zwanenburg A, on behalf of the Imaging Biomarker Standardization Initiative (IBSI). EP-1677: multicentre initiative for standardisation of image biomarkers. *Radiother Oncol*. 2017;123(Suppl 1):S914–S915.
22. Mukaka MM. Statistics corner: a guide to appropriate use of correlation coefficient in medical research. *Malawi Med J*. 2012;24:69–71.
23. Boellaard R, O'Doherty MJ, Weber WA, et al. FDG PET and PET/CT: EANM procedure guidelines for tumour PET imaging: version 1.0. *Eur J Nucl Med Mol Imaging*. 2010;37:181–200.

24. Koo TK, Li MY. A guideline of selecting and reporting intraclass correlation coefficients for reliability research. *J Chiropr Med*. 2016;15:155–163.
25. Parmar C, Grossmann P, Bussink J, Lambin P, Aerts HJWL. Machine learning methods for quantitative radiomic biomarkers. *Sci Rep*. 2015;5:13087.
26. Leijenaar RTH, Nalbantov G, Carvalho S, et al. The effect of SUV discretization in quantitative FDG-PET Radiomics: the need for standardized methodology in tumor texture analysis. *Sci Rep*. 2015;5:11075.
27. van Velden FHP, Kramer GM, Frings V, et al. Repeatability of radiomic features in non-small-cell lung cancer [^{18}F] FDG-PET/CT studies: impact of reconstruction and delineation. *Mol Imaging Biol*. 2016;18:788–795.
28. Altazi BA, Zhang GG, Fernandez DC, et al. Reproducibility of F18-FDG PET radiomic features for different cervical tumor segmentation methods, gray-level discretization, and reconstruction algorithms. *J Appl Clin Med Phys*. 2017;18:32–48.
29. Rahmim A, Qi J, Sossi V. Resolution modeling in PET imaging: theory, practice, benefits, and pitfalls. *Med Phys*. 2013;40:064301.
30. Vandenberghe S, Mikhaylova E, D'Hoe E, Mollet P, Karp JS. Recent developments in time-of-flight PET. *EJNMMI Phys*. 2016;3:3.
31. Orlhac F, Nioche C, Soussan M, Buvat I. Understanding changes in tumor texture indices in PET: a comparison between visual assessment and index values in simulated and patient data. *J Nucl Med*. 2017;58:387–392.
32. Orlhac F, Theze B, Soussan M, Boisgard R, Buvat I. Multiscale texture analysis: from ^{18}F-FDG PET IMAGES TO HISTOLOGIC IMAGES. *J Nucl Med*. 2016;57:1823–1828.
33. Hatt M, Tixier F, Cheze Le Rest C, Pradier O, Visvikis D. Robustness of intratumour ^{18}F-FDG PET uptake heterogeneity quantification for therapy response prediction in oesophageal carcinoma. *Eur J Nucl Med Mol Imaging*. 2013;40:1662–1671.
34. Bashir U, Azad G, Siddique MM, et al. The effects of segmentation algorithms on the measurement of ^{18}F-FDG PET texture parameters in non-small cell lung cancer. *EJNMMI Res*. 2017;7:1–9.
35. Carles M, Torres-Espallardo I, Alberich-Bayarri A, et al. Evaluation of PET texture features with heterogeneous phantoms: complementarity and effect of motion and segmentation method. *Phys Med Biol*. 2017;62:652–668.
36. Cook GJR, Yip C, Siddique M, et al. Are Pretreatment ^{18}F-FDG PET Tumor Textural Features in Non-Small Cell Lung Cancer Associated with Response and Survival After Chemoradiotherapy? *J Nucl Med*. 2013;54:19–26.
37. Tixier F, Le Rest CC, Hatt M, et al. Intratumor heterogeneity characterized by textural features on baseline ^{18}F-FDG PET images predicts response to concomitant radiochemotherapy in esophageal cancer. *J Nucl Med*. 2011;52:369–378.
38. Ha S, Choi H, Cheon GJ, et al., Autoclustering of non-small cell lung carcinoma subtypes on ^{18}F-FDG PET using texture analysis: a preliminary result. *Nucl Med Mol Imaging* (2010). 2014;48:278–286.
39. Kim DH, Jung JH, Son SH, et al. Prognostic significance of intratumoral metabolic heterogeneity on ^{18}f-fdg pet/ct in pathological n0 non-small cell lung cancer. *Clin Nucl Med*. 2015;40:708–714.
40. vanGómez López O, Vicente AMG, Martínez AFH, et al., Heterogeneity in [18 F] Fluorodeoxyglucose positron emission tomography/computed tomography of non–small cell lung carcinoma and its relationship to metabolic parameters and pathologic staging. *Mol Imaging*. 2014;13:7290.2014.00032.

SUPPORTING INFORMATION

Additional supporting information may be found online in the Supporting Information section at the end of the article.

Fig. S1. Percentage of repeatable features discretized with FBW: Percentage of representative features discretized with FBW and segmented based on CT exhibiting an ICC > 0.8 for all studied settings and underlying data categories (from left to right: heterogeneous 3D prints, bigger spheres with high uptake, smaller spheres with high uptake, bigger spheres with low uptake, and smaller spheres with low uptake). TOFM400/P+TM400: TOF/PSF+TOF reconstruction with matrix size 400 × 400.

Fig. S2. Percentage of repeatable features discretized with FBN: Percentage of representative features discretized with FBN and segmented based on CT exhibiting an ICC > 0.8 for all studied settings and underlying data categories (from left to right: heterogeneous 3D prints, bigger spheres with high uptake, smaller spheres with high uptake, bigger spheres with low uptake, and smaller spheres with low uptake). TOFM400/P+TM400: TOF/PSF+TOF reconstruction with matrix size 400 × 400.

Fig. S3. Percentage of repeatable features discretized with FBW: Percentage of representative features discretized with FBW and segmented based on PET exhibiting an ICC > 0.8 for all studied settings and underlying data categories (from left to right: heterogeneous 3D prints, bigger spheres with high uptake, smaller spheres with high uptake, bigger spheres with low uptake, and smaller spheres with low uptake). TOFM400/P+TM400: TOF/PSF+TOF reconstruction with matrix size 400 × 400.

Fig. S4. Percentage of repeatable features discretized with FBN: Percentage of representative features discretized with FBN and segmented based on PET exhibiting an ICC > 0.8 for all studied settings and underlying data categories (from left to right: heterogeneous 3D prints, bigger spheres with high uptake, smaller spheres with high uptake, bigger spheres with low uptake, and smaller spheres with low uptake). TOFM400/P+TM400: TOF/PSF+TOF reconstruction with matrix size 400 × 400.

Table S1. ICC values for all features; extracted from EARL-compliant reconstruction (OSEM, M256, 4 mm FWHM, CT-based segmentation, FBW discretization).

Table S2. ICC values for all features; extracted from EARL-compliant reconstruction (OSEM, M256, 4 mm FWHM, CT-based segmentation, FBN discretization).